The calcined macroporous alumina was amorphous, exhibiting a considerably higher surface area than the zirconia or titania samples. The walls of this sample appeared to be amorphous films by ED and TEM (Fig. 3), yet the 3D packing of the macropores in this sample was similar to that for zirconia and titania. The wall thicknesses, estimated from TEM, varied significantly among the three samples. It is likely that wall thicknesses depend on the individual crystallization kinetics, as well as on any interactions between the latex templates and the inorganic components.

Preliminary experiments have shown that this technique of creating 3D ordered macroporous structures can easily be adapted to oxides of other metals (such as iron and tungsten), phosphates (such as aluminophosphate), and possibly chalcogenides (*18*). It is also possible to create hybrid organic-inorganic wall compositions by using organoalkoxysilanes as precursors, similar to the direct synthesis of mesoporous sieves (*19*). The ease, reproducibility, and versatility of this synthetic approach will facilitate development of new materials and the examination of their structure-property relations. We anticipate that the technique can be modified to include different template sizes. The simplicity of the method suggests that it is amenable to commercial scale-up. Foreseeable technological applications of these materials include quantum optics or optical communications, chromatography, large-molecule catalysis, host-guest systems, thermal or electrical insulators, composites, and porous electrodes or electrolytes.

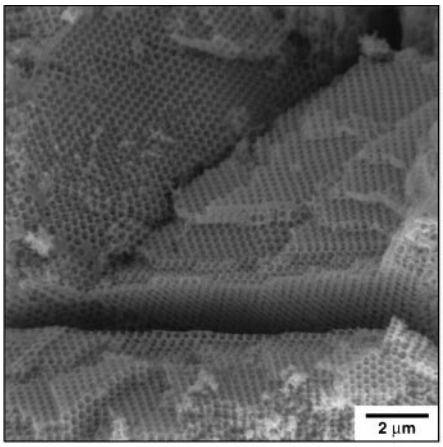

Fig. 2. An SEM image of the calcined macroporous titania sample. The crevice in the center of the image reveals the pore structure in three dimensions. Steps and facets resemble those typically found in crystalline structures. Facets composed of hexagonally close packed voids were most commonly observed.

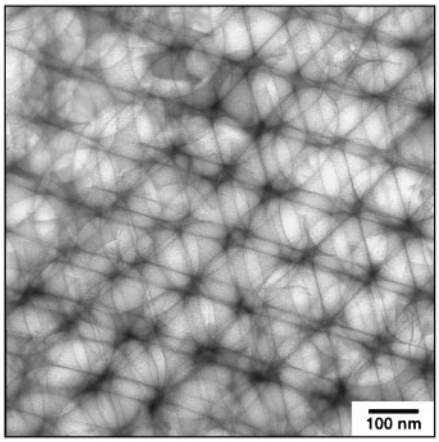

Fig. 3. TEM image of the calcined macroporous alumina sample. No crystalline particles are observed either from bulk PXRD patterns or from SAED patterns.

References and Notes

1. C. T. Kresge, M. E. Leonowicz, W. J. Roth, J. C. Vartuli, J. S. Beck, *Nature* **359**, 710 (1992).
2. A. Monnier *et al.*, *Science* **261**, 1299 (1993).
3. Q. Huo *et al.*, *Nature* **368**, 317 (1994).
4. A. Imhof and D. J. Pine, *ibid.* **389**, 948 (1997).
5. O. D. Velev, T. A. Jede, R. F. Lobo, A. M. Lenhoff, *ibid.* **389**, 447 (1997).
6. M. Antonietti, B. Berton, C. Göltner, H. P. Hentze, *Adv. Mater.* **10**, 154 (1998).
7. M. Templin *et al.*, *Science* **278**, 1795 (1997).
8. D. Zhao *et al.*, *ibid.* **279**, 548 (1998).
9. J. C. Jansen, M. Stöcker, H. G. Karge, J. Weitkamp, Eds., *Advanced Zeolite Science and Applications* (Elsevier, Amsterdam, 1994).
10. G. A. Ozin, *Adv. Mater.* **4**, 612 (1992).
11. E. Yablonovitch, *J. Opt. Soc. Am. B* **10**, 283 (1993).
12. J. D. Joannopoulos, P. R. Villeneuve, S. Fan, *Nature* **386**, 143 (1997).
13. R. H. Perry and D. Green, Eds., *Perry's Chemical Engineers' Handbook* (McGraw-Hill, New York, 1984).
14. M. T. W. Hearn, Ed., *HPLC of Proteins, Peptides and Polynucleotides* (VCH, New York, 1991).
15. C. J. Brinker and G. W. Scherer, *Sol-Gel Science: The Physics and Chemistry of Sol-Gel Processing* (Academic Press, San Diego, CA, 1990).
16. R. L. Fedie, thesis, University of Minnesota, Minneapolis (1996).
17. Scanning electron microscope (SEM) images were recorded digitally on a JEOL 840 SEM operating at 7 kV. Samples were coated with 50 Å of Pt or Pd/Au. Transmission electron microscope (TEM) images were recorded on film on a Philips CM30 TEM operating at 300 kV. Samples were sonicated for 30 min in ethanol and deposited on a holey carbon grid.
18. C. F. Blanford, B. T. Holland, A. Stein, unpublished results.
19. M. H. Lim, C. F. Blanford, A. Stein, *J. Am. Chem. Soc.* **119**, 4090 (1997); *Chem. Mater.* **10**, 467 (1998).

20. Acknowledgment is made to 3M, Dupont, the David and Lucille Packard Foundation, the McKnight Foundation, and NSF (DMR-9701507) for support of this research. We thank W. G. Miller and D. G. Gold for assistance with the latex sphere preparation, and W. L. Gladfelter and M. D. Ward for helpful discussions. B.T.H. and C.F.B. thank the Center for Interfacial Engineering (CIE) at the University of Minnesota for a CIE-NSF graduate fellowship.

7 April 1998; accepted 5 June 1998

A Tunable Kondo Effect in Quantum Dots

Sara M. Cronenwett, Tjerk H. Oosterkamp, Leo P. Kouwenhoven

A tunable Kondo effect has been realized in small quantum dots. A dot can be switched from a Kondo system to a non-Kondo system as the number of electrons on the dot is changed from odd to even. The Kondo temperature can be tuned by means of a gate voltage as a single-particle energy state nears the Fermi energy. Measurements of the temperature and magnetic field dependence of a Coulomb-blockaded dot show good agreement with predictions of both equilibrium and nonequilibrium Kondo effects.

Quantum dots are small solid-state devices in which the number of electrons can be made a well-defined integer N. The electronic states in dots can be probed by transport when a small tunnel coupling is allowed between the dot and nearby source and drain leads. This coupling is usually made as weak as possible to prevent strong fluctuations in the number of confined electrons. A well-defined number of electrons also implies a definite confined charge, that is, N times the elementary charge e. The quantization of charge permits the use of a simple model in which all of the electron-electron interactions are captured in the single-electron charging energy e^2/C, where C is the capacitance of the dot. This simple model has been successful in describing the transport phenomena generally known as single-electron transport and Coulomb blockade effects (*1*).

If the tunnel coupling to the leads is increased, the number of electrons on the dot becomes less well defined. When the fluctuations in N become much greater than unity, the quantization of charge is completely lost. In this open regime, theories of noninteracting electrons usually give a proper description of transport. The theory is more complicated in the intermediate regime where the tunnel coupling is relatively strong but the

S. M. Cronenwett, Department of Applied Physics and DIMES, Delft University of Technology, Post Office Box 5046, 2600 GA Delft, Netherlands, and Department of Physics, Stanford University, Stanford, CA, 94305–4060, USA. T. H. Oosterkamp and L. P. Kouwenhoven, Department of Applied Physics and DIMES, Delft University of Technology, Post Office Box 5046, 2600 GA Delft, Netherlands.

discreteness of charge still plays an important role. Here, the transport description needs to incorporate higher order tunneling processes through virtual, intermediate states. When spin is neglected, these processes are known as cotunneling (*2*). When one keeps track of the spin, it can be convenient to view tunneling as a magnetic-exchange coupling. In this case, the physics of a quantum dot connected to leads becomes similar to the physics of magnetic impurities coupled to the conduction electrons in a metal host, that is, the Kondo effect (*3*, *4*). Recent theory has predicted new Kondo phenomena in quantum dots (*5*–*7*). This spin system allows one to study an individual, artificial magnetic impurity and tune in situ the parameters in the Kondo problem. The first experimental demonstration for a Kondo effect in quantum dots was recently reported by Goldhaber-Gordon and colleagues (*8*). We report here more extensive measurements of the temperature (T) dependence of the equilibrium and nonequilibrium Kondo effect in quantum dots that agree well with the results of (*8*). In addition, we present data using both perpendicular and parallel magnetic fields (B) that unambiguously identify the Kondo physics, and we demonstrate the tunability of the Kondo temperature with an applied gate voltage.

The important parameters for the Kondo effect are illustrated in the energy diagrams of Fig. 1. We treat the dot as an electron box separated from the leads by tunable tunnel barriers with a single spin-degenerate energy state ε_0 occupied by one electron of either spin up or spin down. The addition of a second electron to this state costs an on-site Coulomb energy $U = e^2/C$. First-order tunneling is blocked in the case of Fig. 1A. An electron cannot tunnel onto the dot because the two-electron energy $\varepsilon_0 + U$ exceeds the Fermi energies of the leads, μ_L and μ_R. Also, the electron on the dot cannot tunnel off because $\varepsilon_0 < \mu_L, \mu_R$. This blockade of tunneling is known as the Coulomb blockade (CB) (*1*). In contrast to first-order tunneling, higher order processes in which the intermediate state costs an energy of order U are allowed for short time scales. In particular, we are interested in virtual tunneling events that effectively flip the spin on the dot. One such example is depicted in Fig. 1A (*1*–*3*). Successive spin-flip processes effectively screen the local spin on the dot such that the electrons in the leads and on the dot together form a spin-singlet state. This macroscopically correlated state gives rise to the Kondo effect, which is well known from low-temperature resistivity measurements on metals containing a small fraction of magnetic impurities (*9*). In a quantum dot, the Kondo effect can be described as a narrow peak in the density of states (DOS) at the electrochemical potentials of the leads, $\mu_L = \mu_R$, as shown in Fig. 1B (*5*–*7*). This Kondo resonance gives rise to enhanced conductance through the dot. Out of equilibrium, when a bias voltage V is applied between the source and drain, $eV = \mu_L - \mu_R$, the Kondo peak in the DOS splits into two peaks, each pinned to one chemical potential (Fig. 1C) (*5*, *7*). This splitting leads to two specific features in transport. First, at zero magnetic field, the differential conductance dI/dV versus V mimics the Kondo resonance in the DOS, so a peak in dI/dV is expected around zero voltage. Second, a magnetic field lifts spin degeneracy, resulting in a dI/dV versus V showing two peaks at $eV = \pm g\mu_B \mathbf{B}$ (*5*, *10*), where g is the Landé factor and μ_B is the Bohr magneton.

In our GaAs/AlGaAs quantum dot devices (Fig. 1D), negative voltages applied to the gates control the parameters ε_0, the electron number N, and Γ_L, Γ_R, the energy broadening of the discrete states caused by the coupling to the left and right leads. The conductance shows CB oscillations on varying the gate voltage V_g (for example, Fig. 2A). Although the exact number of electrons N is not known, each period corresponds to a change of one electron on the dot. N should thus oscillate between an even and an odd number. If we assume spin-degenerate filling of the single-particle states (*11*), the total spin on the dot is

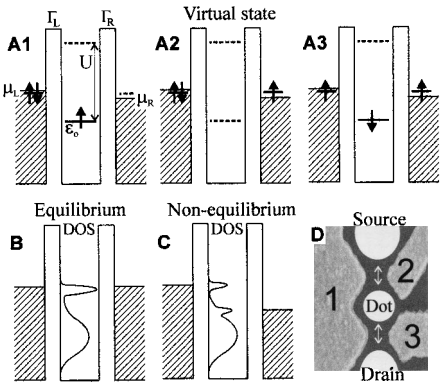

Fig. 1. (**A**) Schematic energy diagram of a dot with one spin-degenerate energy level ε_0 occupied by a single electron; U is the single-electron charging energy, and Γ_L and Γ_R give the tunnel couplings to the left and right leads. The parameters ε_0, Γ_L, and Γ_R can be tuned by the gate voltages. The states in the source and drain leads are continuously filled up to the electrochemical potentials μ_L and μ_R. The series (A1, A2, A3) depicts a possible virtual tunnel event in which the spin-up electron tunnels off the dot and a spin-down electron tunnels on the dot. Such virtual tunnel events, which involve spin-flips, build up a macroscopically correlated state with properties that are known as the Kondo effect. (**B**) The Kondo effect can be pictured as a narrow resonance in the density-of-states (DOS) of the dot at the Fermi energies of the leads, $\mu_L = \mu_R$. The lower energy bump in the DOS is the broadened single-particle state ε_0. (**C**) A source-drain voltage V results in the difference $eV = \mu_L - \mu_R$. For finite V, the DOS peak splits in two; one peak is located at each chemical potential. (**D**) A scanning electron micrograph of the gate structure that defines our quantum dots in the two-dimensional electron gas (2DEG) that is about 100 nm below the surface of a GaAs/AlGaAs heterostructure. Dot 1 has an estimated size of 170 nm by 170 nm and confines ~60 electrons, and dot 2 is about 130 nm by 130 nm and confines ~35 electrons [see (*13*) for more details]. We measured Coulomb oscillations by simultaneously sweeping the voltages on gates 1 and 3.

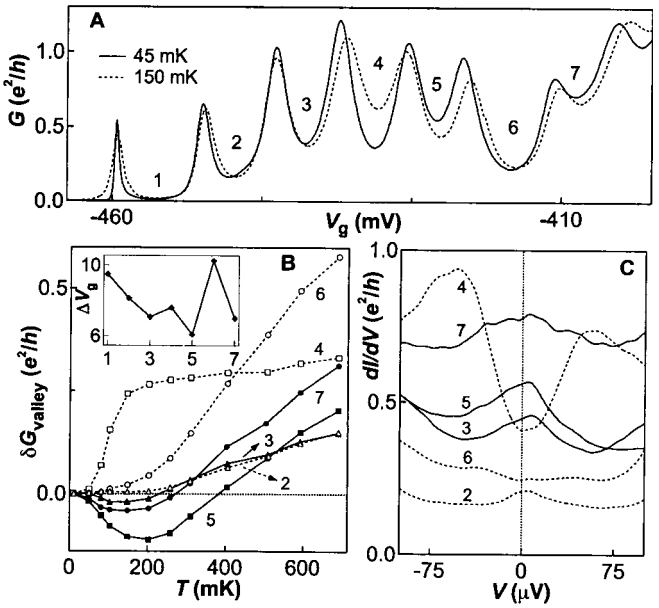

Fig. 2. (**A**) Linear response conductance $G = I/V$ versus gate voltage V_g measured in dot 1 at $B = 0$ for $V = 7.9$ μV at 45 mK (solid) and 150 mK (dashed) (h is Plank's constant). The parity of the electron number in the valleys is indicated by an odd or even number. From left to right, the CB peaks become broader (that is, Γ is increasing) because the tunnel barrier induced by gates 1 and 2 decreases when increasing the voltage on gate 1. Increasing T from 45 to 150 mK increases the conductance of the even-numbered valleys but decreases the conductance of valleys 3, 5, and 7. The detailed temperature dependence is shown in (**B**), where we plot the change in valley conductance $\delta G_{valley}(T) = G_{valley}(T) - G_{valley}(T_{base})$ with $T_{base} \approx 45$ mK. The inset to (B) shows the spacings ΔV_g between adjacent peaks. We observe a larger (smaller) peak spacing for even (odd) N. (**C**) Differential conductance, dI/dV, as a function of V for the center of each CB valley in (A). The odd valleys have a pronounced zero-bias maximum.

zero when N = even (all states are double-occupied with antiparallel spins), and for N = odd the total spin is $\pm$½ (the topmost state is singly occupied with either spin up or down). In other words, for even N the dot is nonmagnetic, whereas for odd N the dot has a net spin magnetic moment (*12*). This property allows quantum dots to be tuned between a Kondo and a non-Kondo system as we vary N with the gate voltage.

Measurements were made on two quantum dots of similar shape (Fig. 1D) (*13*) in a dilution refrigerator with an effective electron base temperature $T_{base} \approx 45$ mK (*14*). The spin-coupling interactions, which give rise to Kondo physics, contribute significantly only for temperatures comparable to or lower than the Kondo temperature $T_K \sim [U\Gamma]^{1/2} \exp[-\pi(\mu-\varepsilon_0)/2\Gamma]$, where $\Gamma = \Gamma_L + \Gamma_R$ (*15*). To make this regime accessible experimentally, Γ is made as large as possible by setting the gate voltages V_g such that the broadened CB oscillations in Fig. 2A slightly overlap. This implies that $\Gamma \sim \Delta$, where Δ is the single-particle level spacing measured as 0.1 and 0.15 meV in dots 1 and 2, respectively (*16*). The respective Coulomb energies U are 1 and 1.3 meV as measured in the weak tunneling regime. In the stronger coupling regime of our measurements, U decreases by a factor of $\sim$2 (*17*).

The dc conductance $G = I/V$ from dot 1 is shown in Fig. 2A for electron temperatures of 45 and 150 mK. The base temperature ($T_{base} \approx 45$ mK) measurement shows even-odd peak spacings (Fig. 2B, inset) that arise from the filling of spin-degenerate energy states. Adding an odd-numbered electron costs $U + \Delta$ in energy, whereas adding an even-numbered electron costs only U. Although the absolute value of N is not exactly known, we obtain the parity of the electron number for the valleys in Fig. 2A from the even-odd spacings together with magnetic field measurements (*11*). Valleys with smaller peak spacings (N = odd) also have a larger base temperature conductance than their neighbors, a result of the Kondo peak in the DOS enhancing the valley conductance when N = odd. Comparing the valley conductances, we see that valleys 3, 5, and 7 decrease when T is increased to 150 mK, whereas the even valleys increase. This even-odd effect is illustrated in more detail in Fig. 2B, where we plot the change in valley conductance with temperature, $\delta G_{valley}(T) = G_{valley}(T) - G_{valley}(T_{base})$. Whereas all the valley conductances for N = even increase with T, for N = odd the spin-correlation is destroyed by increasing T such that δG_{valley} first decreases. The minimum in δG_{valley} strongly resembles the resistance minimum in metallic Kondo systems (*9*).

Measurements on dot 2 also show agreement with expectations of the Kondo effect. The middle valley in Fig. 3A is identified as a "Kondo" valley because it shows a larger base temperature conductance than the neighboring valleys. The detailed T dependence in Fig. 3B shows that this Kondo valley also has a minimum conductance around 200 mK. Furthermore, the conductance peaks on either side of the Kondo valley decrease and move apart with increasing T (see also Fig. 3B) in qualitative agreement with theory (*5*). The motion of the peak position, which has not been previously reported, is attributed to a renormalization of the noninteracting energy state ε_0 due to fluctuations in N.

To investigate the nonequilibrium Kondo effect, we measured the differential conductance dI/dV in the center of the Kondo valley of Fig. 3A. At base temperature, dI/dV has a peak at $V = 0$ (Fig. 3C, bold curve). The peak has a width of $\sim$50 μV, which is narrow compared to the energy scales of U, Δ, and Γ. Increasing T broadens the dI/dV peak until it completely disappears at $\sim$300 mK. The insets to Fig. 3C give the T dependence of the dI/dV peak maximum on a logarithmic scale and the peak width (the full-width at three-quarters maximum) on a linear scale. The logarithmic T dependence of the maximum is expected for $T_K \lesssim T$ (*3*). At low temperatures, the width is expected to saturate at $\sim T_K$. We do not observe such saturation, which suggests that $T_K \lesssim 45$ mK in the middle of the Kondo valley.

In order to increase $T_K \sim [U\Gamma]^{1/2} \exp[-\pi(\mu-\varepsilon_0)/2\Gamma]$, we decrease the distance between ε_0 and the Fermi energy by moving away from the Kondo valley toward a neighboring CB peak. The zero-bias dI/dV peak is seen to increase in both height and width when tuning ε_0 toward the Fermi energy (Fig. 3D). The width of the dI/dV peak, shown in Fig. 3E, is determined by the larger of T_K or T. The increase in width when approaching the CB peaks on either side of the Kondo valley indicates that here T_K exceeds T. Figure 3E demonstrates the first control of T_K in

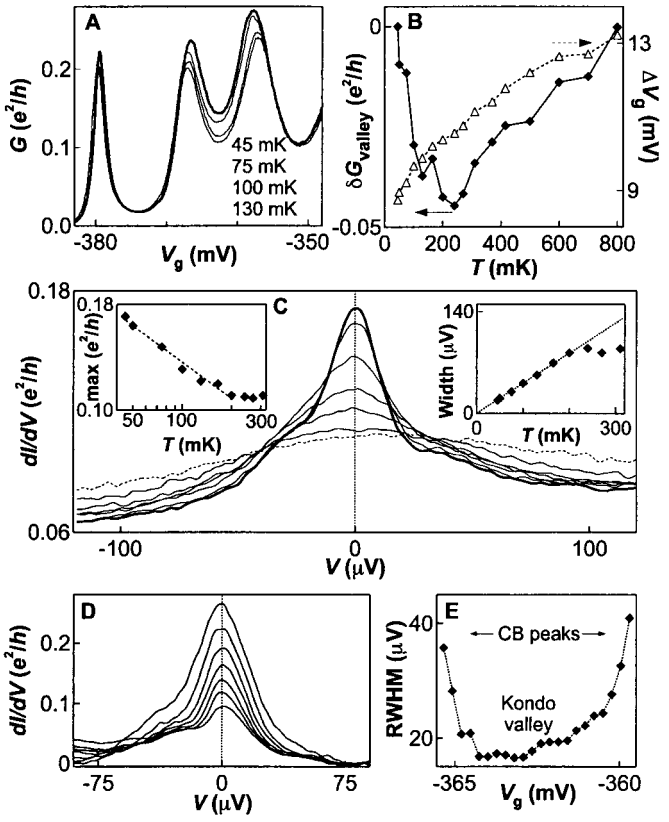

Fig. 3. (**A**) Conductance G for $B = 0$ and $V = 5.9$ μV at 45 (bold curve), 75, 100, and 130 mK in dot 2. Because dot 2 is smaller, the tunnel barriers increase more rapidly with negative gate voltage, and we observe only three consecutive valleys in the Kondo regime. The middle valley shows pronounced Kondo behavior. The remainder of this figure shows the dependence on T, V, and ε_0. (**B**) Left axis: $\delta G_{valley}(T)$ (◆) for the center of the middle Kondo valley in (A). Right axis: Gate-voltage spacing $\Delta V_g(T)$ of the peaks bordering the Kondo valley. Increasing T results both in a Kondo minimum in δG_{valley}, and an increasing peak spacing that we ascribe to a renormalization of the energy level ε_0. (**C**) Differential conductance dI/dV versus V for T = 45 (bold), 50, 75, 100, 130, 200, and 270 (dashed) mK. The gate voltage is set in the center of the middle valley. The peak maximum (left inset) is logarithmic in T. The peak width (the full-width at three-quarter maximum, right inset) is linear in T with a slope of $4.8k_B$ (dotted line) (k_B is Boltzmann's constant). The asymmetry in the zero-bias peak is probably because $\Gamma_L \neq \Gamma_R$. (**D**) Zero-bias peak in dI/dV at 45 mK for different gate voltages stepping from the center of the Kondo valley in (A) (bottom curve, $V_g = -363$ mV) up the left side of the CB peak (top curve, $V_g = -366$ mV). The curves have been shifted so the background values align at $\sim$75 μV. The amplitude of the zero-bias peak increases as the conductance G increases moving up the flank of the CB peak. (**E**) We measure the right half-width at half-maximum (RWHM) of the zero-bias peak (relative to the baseline dI/dV at $\sim$75 μV), which begins to increase halfway up the CB peak on either side. The increasing width follows the increase of T_K above T_{base}. The increase in T_K results from bringing ε_0 toward the Fermi energies $\mu_L = \mu_R$ by tuning the gate voltages.

a Kondo system. The largest value we obtained for T_K can be estimated from the largest *dI*/*dV* peak in Fig. 3D; the width of ≈80 μV implies $T_K \sim 1$ K.

The absence and presence of a zero-bias peak for N = even or odd, respectively, can be seen in the *dI*/*dV* measurements for the valleys of dot 1 in Fig. 2C. Valleys 3, 5, and 7 indeed have a narrow zero-bias peak. Valley 4 has a minimum in the *dI*/*dV* (*18*), whereas valley 6 has a flat *dI*/*dV*. Valley 2 shows a slight maximum at $V = 0$. This could arise from a dot with a net spin of ±1 instead of 0. Occasionally we observed small shoulders on the sides of peaks in *dI*/*dV*. It is unclear whether these shoulders are related to the presence of multiple levels in our dots (*16*).

A magnetic field $B_\parallel$ in the plane of the two-dimensional electron gas (2DEG) splits the spin-degenerate states of the quantum dot by the Zeeman splitting, $\varepsilon_\pm = \varepsilon_0 \pm g\mu_B B_\parallel/2$. When the dot has an unpaired electron, the Kondo peak in the DOS at each chemical potential is expected to split by twice the Zeeman energy, $2g\mu_B B_\parallel$ (*5*). In equilibrium, there is no longer a peak in the DOS at $\mu_L = \mu_R$, and the zero-bias conductance is not enhanced. Instead, one expects the peak in *dI*/*dV* to be shifted to a finite bias $V = \pm g\mu_B B_\parallel/e = \pm 25$ μV/T, where $g = -0.44$ for bulk GaAs. In Fig. 4A we show that indeed the zero-bias peak splits into two peaks when we increase $B_\parallel$ from 0 to 7 T. The peak positions, shown in Fig. 4B, fall directly on top of the theoretical prediction, ±25 μV/T (dashed lines) (*19*).

The correct splitting of the *dI*/*dV* peak with magnetic field is considered as the most distinct sign of Kondo physics (*5*). Probing the Zeeman doublet single-particle state with the differential conductance could also reveal a peak split linear in $B_\parallel$. However, in this case, the splitting is gate-voltage dependent. A gate voltage–independent peak split by $2g\mu_B B_\parallel$ distinctively identifies the Kondo effect with no free parameters. Figure 4, D and E, shows a gray-scale plot of *dI*/*dV* as a function of V and V_g over a Kondo valley. The maxima of the CB peaks (horizontal) and the Kondo *dI*/*dV* peak (vertical) are indicated by dashed lines. In Fig. 4, D and E, the maxima in *dI*/*dV* occur only for the Kondo valley and not for the neighboring valleys. The locations of the split maxima for $B_\parallel = 1.5$ T are independent of V_g throughout the valley.

Peaks in *dI*/*dV* reported in (*8*) were split by 33 μV/T in a magnetic field $B_\perp$ perpendicular to the plane of 2DEG. This value, significantly less than the expected 50 μV/T, could result from quantum Hall states in the leads. Figure 4C shows the *dI*/*dV* at $B_\perp = 1.89$ T for both our quantum dot (solid) and a single quantum point contact (dashed). Each curve shows split peaks in *dI*/*dV* at 36 μV/T. The point contacts of both our dots showed significant structure around ~35 μV/T in a perpendicular magnetic field. What might cause a field-dependent splitting in the *dI*/*dV* of a quantum point contact is unclear. However, the orbital changes caused by $B_\perp$ severely complicate the identification of Kondo physics in a perpendicular magnetic field. Furthermore, with the formation of spin-polarized Landau levels in the leads, a single electron on the dot cannot equally couple to both spin states in the leads, which should suppress the Kondo resonance.

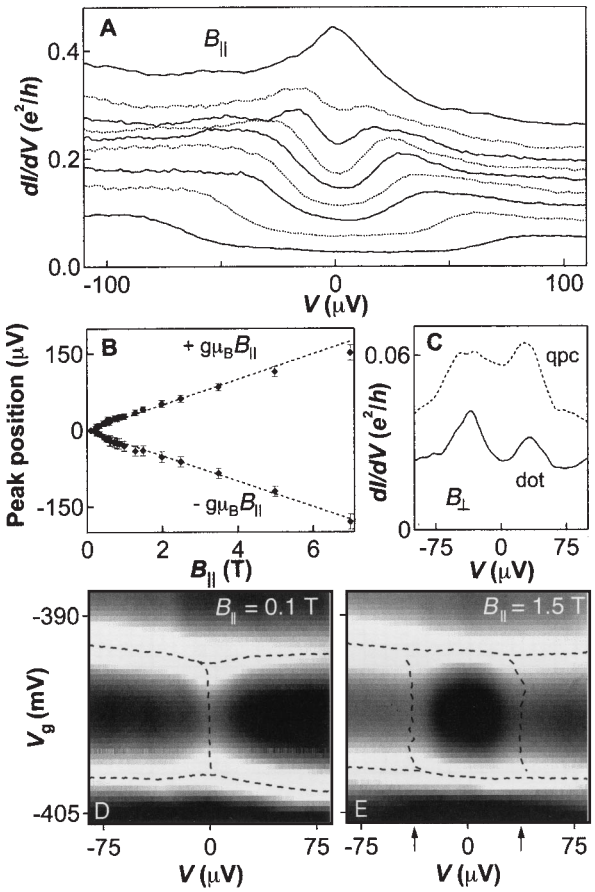

Fig. 4. (**A**) The splitting of the zero-bias peak in the differential conductance *dI*/*dV* with a magnetic field $B_\parallel$ in the plane of the 2DEG; from top to bottom: $B_\parallel$ = 0.10, 0.43, 0.56, 0.80, 0.98, 1.28, 1.48, 2.49, and 3.49 T. The curves are offset by 0.02 e^2/h. Above ~0.5 T, we resolve a splitting that increases linearly with $B_\parallel$. The data are from the Kondo valley of Fig. 3A. (**B**) Position, in bias voltage, of the *dI*/*dV* maxima as a function of $B_\parallel$ up to 7 T. The dashed line indicates the theoretical splitting of $\pm g\mu_B B/e = \pm 25$ μV/T with $g = -0.44$ for GaAs. (**C**) Split peaks at 36 μV/T are observed in the *dI*/*dV* of the quantum dot and also in a single point contact (qpc) (formed by a negative voltage on gates 1 and 3 only) in a perpendicular magnetic field $B_\perp = 1.89$T. The Landau level filling factor is 4 at this field in the bulk 2DEG. Measurements at other $B_\perp$ and in other qpc's also showed similar structure. In contrast, the *dI*/*dV* of a qpc in high $B_\parallel$ is flat. (**D** and **E**) Gray-scale plots of *dI*/*dV* as a function of V_g and V show the zero-bias peak for $B_\parallel = 0.1$ T split into two shoulder peaks at $B_\parallel = 1.5$ T. The contour of the CB peaks (horizontal) and the maxima in the *dI*/*dV* (vertical) are indicated by dashed lines. The valleys on either side of the Kondo valley do not show a zero-bias or split *dI*/*dV* peak. The arrows on the bottom axis of (E) indicate the theoretical splitting, which should be independent of V_g, with a value of ±37.5 μV at $B_\parallel = 1.5$ T. The arrows match the experimental results very well.

References and Notes

1. For a review, see L. P. Kouwenhoven *et al.*, in *Mesoscopic Electron Transport, Proceedings of a NATO Advanced Study Institute*, L. L. Sohn, L. P. Kouwenhoven, G. Schön, Eds., (Kluwer, Dordrecht, Netherlands, 1997), ser. E, vol. 345, pp. 105–214; available at: http://vortex.tn.tudelft.nl/~leok/papers/
2. For a review on cotunneling, see D. V. Averin and Y. V. Nazarov, in *Single Charge Tunneling, Proceedings of a NATO Advanced Study Institute*, H. Grabert and M. H. Devoret, Eds. (Plenum, New York, 1991), ser. B, vol. 294, pp. 217–247.
3. L. I. Glazman and M. É. Raikh, *Pis'ma Zh. Eksp. Teor. Fiz.* **47**, 378 (1988) [*JETP Lett.* **47**, 452 (1988)].
4. T. K. Ng and P. A. Lee, *Phys. Rev. Lett.* **61**, 1768 (1988); A. Kawabata, *J. Phys. Soc. Jpn.* **60**, 3222 (1991).
5. Y. Meir, N. S. Wingreen, P. A. Lee, *Phys. Rev. Lett.* **70**, 2601 (1993); N. S. Wingreen and Y. Meir, *Phys. Rev. B* 49, 11040 (1994).
6. S. Hershfield, J. H. Davies, J. W. Wilkins, *Phys. Rev. Lett.* **67**, 3720 (1991).
7. J. König, J. Schmid, H. Schoeller, G. Schön, *Phys. Rev. B* **54**, 16820 (1996); for further references, see H. Schoeller, in *Mesoscopic Electron Transport, Proceedings of a NATO Advanced Study Institute*, L. L. Sohn, L. P. Kouwenhoven, G. Schön, Eds. (Kluwer, Dordrecht, Netherlands, 1997), ser. E, vol. 345, pp. 291–330.
8. D. Goldhaber-Gordon *et al.*, *Nature* **391**, 156 (1998).
9. J. Kondo, in *Solid State Physics*, H. Ehrenreicht, F. Seitz, D. Turnbull, Eds. (Academic Press, New York, 1969), vol. 23, p. 183–281.
10. D. C. Ralph and R. A. Buhrman, *Phys. Rev. Lett.* **72**, 3401 (1994); I. K. Yanson *et al.*, *ibid.* **74**, 302 (1995).
11. In measurements of the evolution of the CB peaks versus B, we observe pairing in the motion between adjacent peaks. This indicates spin-degenerate filling of the energy states, in contrast to the results of D. R. Stewart *et al.* [*Science* **278**, 1784 (1997)], who reported non–spin-degenerate filling of the energy states.
12. Y. Wan, P. Phillips, Q. Li, *Phys. Rev. B* **51**, 14782 (1995).
13. The two quantum dots form the double dot structure discussed in detail by N. C. van der Vaart *et al.* [*Phys. Rev. Lett.* **74**, 4702 (1995)]. Each dot was measured independently by biasing only the gate voltages that define a single dot.
14. Measurements were made with a variable dc bias. For *dI*/*dV* traces, an ac bias of 1 μV at 13.5 Hz was added

for lock-in detection. The effective electron base temperature, $T_{base} \approx 45$ mK, was measured from CB peak widths in the weak tunneling regime.

15. N. E. Bickers, *Rev. Mod. Phys.* **59**, 845 (1987).
16. The presence of more than one state in our dots is expected to enhance the Kondo temperature. For an analysis of multiple-level effects, see T. Inoshita *et al.*, *Phys. Rev. B* **48**, 14725 (1993); T. Inoshita, Y. Kuramoto, H. Sakaki, *Superlattices Microstruct.* **22**, 75 (1997); T. Pohjola *et al.*, *Europhys. Lett.* **40**, 189 (1997).
17. E. B. Foxman *et al.*, *Phys. Rev. B* **47**, 10020 (1993).
18. The *dI*/*dV* minimum of valley 4 resembles the form predicted by J. König, H. Schoeller, and G. Schön [*Phys. Rev. Lett.* **76**, 1715 (1996)] for a quantum dot with N = even.
19. Our data fit well to the theoretical predictions when we use the g factor for bulk GaAs, $g = -0.44$, whereas the g factor in the 2DEG of a typical GaAs/AlGaAs heterostructure has been experimentally determined to be less than in the bulk by M. Dobers, K. v. Klitzing, and G. Weimann [*Phys. Rev. B* **38**, 5453 (1988)].
20. We thank R. Aguado, B. Broer, L. I. Glazman, S. F. Godijn, K. K. Likharev, C. M. Marcus, J. E. Mooij, and N. C. van der Vaart for help and discussions and Philips Laboratories and C. T. Foxon for providing the heterostructure. Supported by the Dutch Foundation for Fundamental Research on Matter (FOM), the Royal Netherlands Academy of Arts and Sciences (L.P.K.), and the NSF under grant DMR-945805 (S.M.C.).

30 March 1998; accepted 2 June 1998

Mass-Independent Oxygen Isotope Fractionation in Atmospheric CO as a Result of the Reaction CO + OH

T. Röckmann, C. A. M. Brenninkmeijer, G. Saueressig, P. Bergamaschi, J. N. Crowley, H. Fischer, P. J. Crutzen

Atmospheric carbon monoxide (CO) exhibits mass-independent fractionation in the oxygen isotopes. An ^{17}O excess up to 7.5 per mil was observed in summer at high northern latitudes. The major source of this puzzling fractionation in this important trace gas is its dominant atmospheric removal reaction, CO + OH $\rightarrow$ CO_2 + H, in which the surviving CO gains excess ^{17}O. The occurrence of mass-independent fractionation in the reaction of CO with OH raises fundamental questions about kinetic processes. At the same time the effect is a useful marker for the degree to which CO in the atmosphere has been reacting with OH.

Small variations in isotopic composition occur throughout nature and often give useful information about physical, chemical, and biological processes. The various underlying isotope fractionation effects are normally proportional to isotopic mass differences (*1*); however, isotope fractionation effects have recently been discovered that do not depend on the mass of the substituted isotope (*2–10*). The causes of the sometimes exceptionally strong mass-independent fractionation (MIF) are complex and not yet understood. In the atmosphere MIF is widespread, and each of the important trace gases—O_3 (*2, 6*), CO_2 (*7*), CO (*5, 8, 9*) and N_2O (*10*)—has excess ^{17}O, which for oxygen is an excellent marker for MIF. The clearest case of MIF occurs in atmospheric O_3, in which both ^{17}O and ^{18}O are nearly equally enhanced relative to its precursor, atmospheric O_2. This is in contrast to most other oxygen-bearing compounds on Earth for which $\delta^{17}O = 0.52 \times \delta^{18}O$ (*11*). For MIF, $\Delta^{17}O \equiv \delta^{17}O - 0.52 \times \delta^{18}O \neq 0$.

MIF in CO was discovered from analysis of samples collected in New Zealand (*8*). Subsequent measurements established that it is a widespread phenomenon, and initially the effect was linked to MIF in O_3 (*5*). The reaction of O_3 with unsaturated hydrocarbons, mainly isoprene and terpenes emitted by plants, indeed produces CO that inherits the relatively strong MIF in O_3 of 25 to 40 per mil (*5, 6*). However, despite the large $\Delta^{17}O(O_3)$ value, there is insufficient CO from this source to explain the observed $\Delta^{17}O(CO)$ values in remote air masses (*5*).

Our measurements reveal that $\Delta^{17}O(CO)$ values at high northern latitudes vary seasonally (Fig. 1). In winter, CO in clean surface air at Alert and Spitsbergen peaks at about 170 ppb. Removal rates for reaction with hydroxyl (OH) are low, the sources outweigh the sink, and the isotopic composition of the accumulating CO reflects that of the combined sources. Because fossil fuel combustion is an important source of CO, $\delta^{18}O$ values are high (*12*) and $\Delta^{17}O(CO)$ values are low (*5*). During spring and summer, oxidative cleaning of the atmosphere by OH gathers momentum and CO levels decline. Concurrently $\delta^{18}O$ values decrease because of the inverse kinetic isotope effect (*13*) and the diminished role of fossil fuel sources (*12*). In contrast, $\Delta^{17}O(CO)$ values reach their highest levels when OH peaks in summer, implicating the reaction between CO and OH as a possible source of MIF.

To investigate MIF in this reaction, we saturated a mixture of ~1% CO in He or N_2 as the bath gas with H_2O_2 vapor and circulated the mixture through a photochemical reactor in which OH was produced from photolysis of H_2O_2 with a Xe lamp (wavelength $\lambda > 190$ nm). After a reaction time of 15 to 90 min, typically 15 to 65% of the original CO had been oxidized, and the residual CO was analyzed for its $^{13}C/^{12}C$ and $^{18}O/^{16}O$ ratio by mass spectrometry (*12, 14*). For $^{17}O/^{16}O$ analysis, samples were first converted to O_2 with a F_2-based technique (*15*). With this method $^{17}O/^{16}O$ variations can be resolved from the strongly interfering $^{13}C/^{12}C$ variations. The results show that the remaining CO fraction progressively obtains excess ^{17}O (Fig. 2). The effect diminishes at lower pressures and also when He is used as a bath gas. The equilibrium fractionation, plotted versus pressure in Fig. 3, was derived from the slopes of the linear fits in Fig. 2.

To ascertain that the MIF observed here exclusively arises from the chemical reaction of CO with OH, we need to exclude possible interferences. An alternative mechanism would be transfer of MIF from OH to CO through isotopic exchange. However, measurements confirm that the H_2O_2 used and consequently the OH formed is free of MIF. Furthermore, there exists experimental and theoretical evidence against significant oxygen isotope exchange in the reaction between CO and OH (*16*).

The generation of MIF in CO by means of exchange with OH is excluded in the troposphere as well (*5*). Although atmospheric OH is mainly produced by the reaction $O(^1D) + H_2O \rightarrow 2$ OH, and initially must reflect the strong MIF of O_3 [the $O(^1D)$ precursor], fast exchange with H_2O according to OH + H_2O $\leftrightarrow$ H_2O + OH efficiently washes the MIF signal out (*17*).

Other potential interfering agents in our experiments were $O(^3P)$ or $O(^1D)$, which could cause MIF by exchange or reaction with CO. Whether or not O_2 is excluded from the experiments, some is inevitably produced by thermal decomposition of H_2O_2 and the photochemical reactions involving OH, HO_2, and H_2O_2. Experiments with the addition of 10 to 20% O_2, with and without H_2O_2, confirm that MIF in the remaining CO only occurs when H_2O_2 is present.

An independent check on our experiments

Max Planck Institute for Chemistry, Atmospheric Chemistry Division, Postfach 3060, 55020 Mainz, Germany.